Chapter 1
Fundamentals of Microchannels

Abstract The growing demand for product miniaturization in all industrial sectors, coupled with global competition for more reliable, faster, and cost-effective products, has led to many new challenges for design and operation of thermal management systems. The rapid increase in the number of transistors on microchips, with increased functionality/power and consequently higher heat fluxes, is one such great challenge in the electronics packaging industry. Microchannel heat and mass exchanger technologies are finding new applications in diverse industries and emerging as a promising solution to game changing technologies in the way we design and operate next-generation, high performance thermal management systems. The discussion in this chapter will deal with fundamentals of microchannels. We begin by introducing the history, technical background, classification, advantages, and disadvantages of microchannels. Fabrication methods (conventional technology and modern technology) for microchannels are considered next. Finally, correlations of pressure drop and heat transfer coefficient for single-phase and phase-change flows are presented for a variety of internal flow conditions.

Keywords Fabrication · Micro heat and mass exchangers · Pressure drop · Heat transfer · Phase change · Two-phase · Correlations

1.1 Introduction and History of Microchannels

1.1.1 History

A great deal of work has been conducted on single-phase heat transfer in microchannels since Tuckerman and Pease's pioneering effort (1981) on the cooling of very large-scale integrated circuits (VLSI). In early 1981, Tuckerman and Pease

M. Ohadi et al., *Next Generation Microchannel Heat Exchangers*,
SpringerBriefs in Thermal Engineering and Applied Science,
DOI: 10.1007/978-1-4614-0779-9_1, © The Author(s) 2013

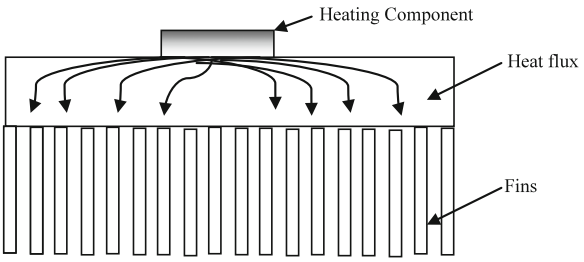

Fig. 1.1 Diagram showing scale of components and cooling system (Zang et al. 2003)

(1981) first explained the concept of microchannel heat sinks and predicted that single-phase forced convective cooling in microchannels could potentially remove heat at a rate of the order of 1,000 W/m^2.

Forced convection in channels and liquid injection has been used for faster and larger scale cooling in industry for decades. Microchannel heat transfer, however, has become increasingly popular and interesting to researchers due to high heat transfer coefficients, with potential for record-high heat transfer coefficient and low to moderate pressure drops when compared to conventional air and liquid cooled systems (Philips 1988; Gillot et al. 2000; Hsu et al. 1995; Hahn et al. 1997; Martin et al. 1995; Viday et al. 1993). For example, microchannel heat sinks have been demonstrated for high-power laser diode array cooling and have achieved a heat flux removal rate of 500 W/cm^2 (Missaggia et al. 1989; Mundinger et al. 1988; Beach et al. 1992). Figure 1.1 shows the proposed design of a two-phase microchannel heat sink fabricated on the backside of a flip chip-bonded IC chip (Zang et al. 2003). In the last few decades, studies on two-phase flow and heat transfer characteristics in microchannel flow passages have become increasingly important due to the rapid development of micro-devices used for various engineering applications, such as medical devices, high heat flux compact heat exchangers, and cooling of high-power density micro-electronics, supercomputers, plasma facing components, and high-powered lasers. The continuing push toward more densely packed microchips may require greater heat dissipation than that typically provided by simple forced air-cooling systems. Liquid cooling using microchannels integrated with microchips is the next most attractive alternative (Schmidt 2003).

1.1.2 Introduction of Microchannels

In most cases when cooling requirements are over 100 W/cm^2 they cannot be easily met either by simple air-cooling or water-cooling systems. In many applications, to dissipate the high heat flux of the components, the required heat sinks must be larger than the components themselves, as shown in Fig. 1.1. Nevertheless, hot spots usually appear, and non-uniform heat flux levels are observed at the heat sink level. This has motivated researchers to develop new heat sinks that can

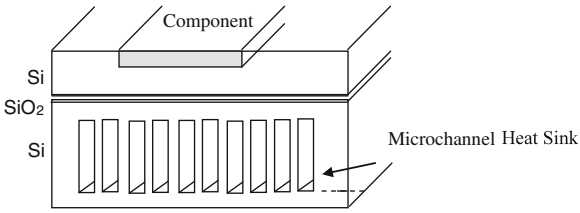

Fig. 1.2 Silicon microchannel heat sink with heating component for cooling (Gillot et al. 2001)

be directly embedded on the back of the heat source for uniform heat flux removal, as shown in Fig. 1.2. This heat sink is usually made out of silicon, with a silicon oxide layer to keep the component electrically insulated. Very narrow rectangular channels are formed with fins in the micrometer range that ensure uniform heat flux removal by circulating cold fluid through the rectangular microchannels.

From Newton's law of cooling we know that for a fixed temperature difference, heat flux depends on the product of hA, where h is the heat transfer coefficient and A is the heat transfer surface area. So, in order to fulfill the requirement of high heat flux removal the product of hA has to be increased, and since the heat transfer coefficient h is related to the hydraulic diameter, increasing surface area is one option. The heat transfer area can be increased by using microchannels on the heat generating body (chip surface), as shown in Fig. 1.2. The flow behavior of water inside the channels is determined by the channel hydraulic diameter and the channel cross-sectional area. To obtain high heat transfer, a smaller hydraulic diameter and a larger heat transfer area of the channel are preferred, so a number of narrow channels with high depth are suitable. Smaller hydraulic diameter and larger cross-sectional area increase the pressure drop and consequently require higher pumping power. On the other hand, increased cross-sectional area of the heating surface enhances the heat transfer rate. These requirements can be adjusted with next-generation microchannels that will have larger hydraulic diameter but provide larger cross-sectional area as well as high heat transfer coefficient.

1.1.3 Classification of Microchannels/Minichannels

We can classify microchannels in different ways. Several investigators have proposed different criteria for minichannels vs. microchannels. Serizawa et al. (2002) described one criterion for classification of microchannels proposed by Suo and Griffith (1964) as follows:

$\lambda \geq d_h$ where λ is the Laplace constant and d_h is the channel diameter.

Mehendale et al. (2000) used the hydraulic diameter to classify micro heat exchangers as follows:

- Micro heat exchanger: 1 μm $\leq d_{\mathrm{h}} \leq$ 100 μm
- Meso-heat exchanger: 100 μm $\leq d_{\mathrm{h}} \leq$ 1 mm

- Compact heat exchanger: 1 mm $\leq d_h \leq$ 6 mm
- Conventional heat exchanger: $d_h >$ 6 mm

Kandlikar (2002) proposed a microchannel classification for single-phase as well as two-phase applications as follows:

- Conventional channels: $d_h >$ 3 mm
- Minichannels: 3 mm $d_h >$ 200 μm
- Microchannels: 200 μm $d_h >$ 10 μm

Palm (2000) gave a more general definition of microchannels, describing them as heat transfer elements where the classical theories cannot correctly predict the friction factor and heat transfer. Stefan (2002) defined a microscale system as one whose typical phenomena are absent in a macro system. So it is not always suitable to differentiate mini- and microchannels by a specific diameter such as hydraulic diameter of 1 mm, although this definition is often used nonetheless.

1.1.4 Benefits and Challenges of Microchannels

Flow in microchannels has been widely investigated during the last two decades in the search for effective, faster cooling of high-power density electronic devices. As discussed above, the advantage of microchannels lies in their high heat transfer coefficient and ability to decrease the size of heat exchangers significantly. Other advantages are their reduced weight, low inventory, and reduced use of materials. The decreased diameters of microchannels result in more compact heat exchangers and higher heat transfer coefficients through more surface area per unit volume. Microchannels have wide practical applications in highly specialized fields, such as bioengineering and microfabricated fluidic systems, micropumps, and micro-heat pipes. For example, the compactness and low weight of microchannels have turned the automotive industry toward micro heat exchangers, and today microchannels have almost completely replaced circular tubes in automotive condensers and heat exchangers with hydraulic diameters of around 1 mm. More recently, microchannels have been successfully applied to automotive air conditioning systems, fuel cells, and microelectronics. The main challenges of microchannels are the fabrication difficulties and high-grade filtering of the working fluid necessary for it to flow through the channels. High pressure drop and the pumping power required are also considered challenges of microchannels.

1.2 Fabrication Methods for Microchannels

Microchannels are fabricated by a variety of processes depending on the dimensions and materials used. Common materials used for microchannels are silicon, silica, polycarbonate/polyimide, plastic, or metal. Basic microchannel configurations are

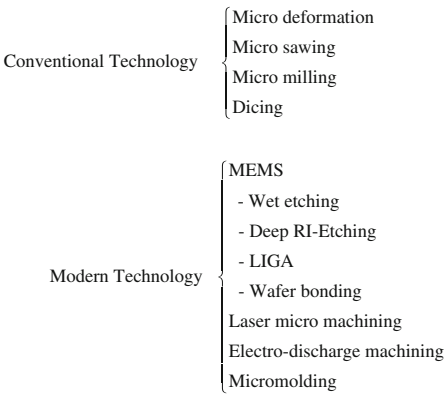

Fig. 1.3 Taxonomic chart of fabrication methods for microchannels

rectangular, semicircular, triangular, or trapezoidal cross-sections, which are widely reported in the literature and are summarized by Nguyen and Werely (2002). Other geometrically complex microchannels may offer more attractive performance, but they have not yet been investigated. Since the first demonstration of microchannels by Tuckerman and Pease (1981), a number of microchannel fabrication methods have become standard processing approaches in this field. These methods can be divided into two groups, conventional technologies and modern technologies, as shown in Fig. 1.3. Conventional fabrication technologies include methods such as micro-deformation, micro-sawing, micro-milling, and dicing. Modern microchannel fabrication techniques include MEMS (Micro-Electro-Mechanical Systems) methods, laser micro-machining, electro-discharge machining, and micro-molding. MEMS technology has grown dramatically alongside semiconductor technology and is the most widely used technology in research laboratories. Recently, laser micro-machining technology has gained the spotlight due to the method's low manufacturing uncertainty and its potential to manufacture an unlimited number of geometries. This section will focus on micro-deformation, micro-sawing, deep RI-etching, and laser micro-machining technologies, which are widely used in manufacturing. Table 1.1 presents a summary of some fabrication methods for microchannels. Detailed explanations of the fabrication methods will be provided in the following sections.

1.2.1 Conventional Technology

1.2.1.1 Micro-Deformation

As indicated in Table 1.1, the micro-deformation technique can fabricate rectangular channels on any material. As reported by Kukowski (2003), the micro-deformation process can form up to 500 channels per inch. At this time, microchannels of up to 250 channels per inch are routinely formed on a broad

Table 1.1 Summary of some fabrication methods for microchannels

	Micro-deformation technology	Micro-machining	MEMS (Deep reactive ion etching)	Laser micro-machining
Geometries	Rectangular	Rectangular	Rectangular, circular, triangular, trapezoidal	Unlimited
Materials	Metal and non-metal	Metal and silicon	Metal, silicon, and glass	Metal and glass
Channel range	250 channels/inch	0.1–10 mm	Nanometer scale to millimeter scale	Nanometer scale to millimeter scale
Advantages	Low cost, fast	High or low aspect ratio, inexpensive, fast	Low manufacturing uncertainty	Low manufacturing uncertainty
Disadvantages	Some materials require post-treatment	Complex design is impossible	Slow process (1 day)	Too expensive

range of materials. The channels are cut in one continuous pass or multiple passes depending on the system used. The advantages of the micro-deformation technology include low cost and quickness. However, depending on the strain-hardening rate of the materials, some processed materials after micro-deformation processing may require additional post treatment.

As shown in Fig. 1.4, the working principles of the micro-deformation technology are simple. Using the patented tool and prescribed interference angles with the work piece, the process plastically deforms ductile materials. The tool moves the base material, and depending on the geometric configuration of the tool, plastically deforms that material to the defined and repeatable shape. Only one tool is required for each desired configuration. The tool with one-point landing channels the material while deforming or lifting the material to the desired geometric shape and angle, simultaneously finning and forming microchannels of a variety of repeatable contours and dimensions.

1.2.1.2 Micro-Sawing

Micro-sawing is a technique widely used in industry that can fabricate rectangular channels in metal or silicon with an applicable channel width in the range of 0.1–10 mm. This technology can fabricate microchannels with high or low aspect ratios. It is very fast and has the lowest manufacturing cost among all micro-fabrication technologies. The technology uses a fret saw to fabricate rectangular microchannels, such as those shown in Fig. 1.5.

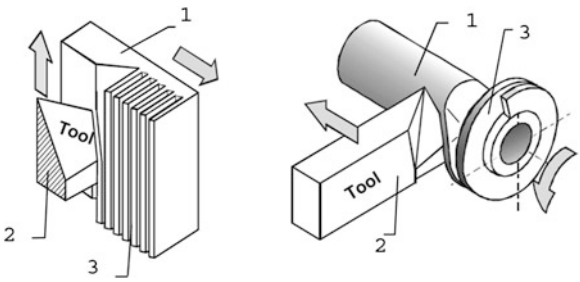

Fig. 1.4 Working principle of micro-deformation technology: *1* work piece, *2* cutting tool, *3* section with microchannels (Kukowski 2003)

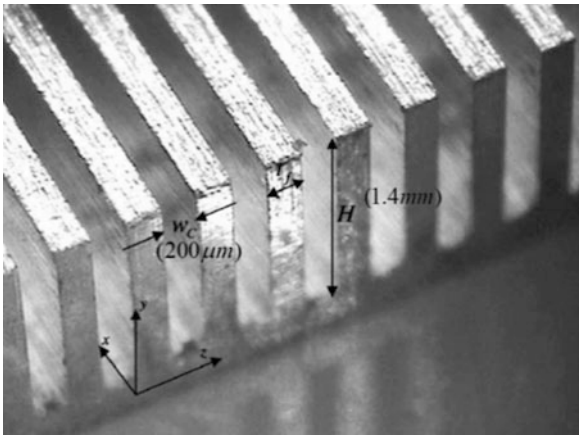

Fig. 1.5 Microchannels manufactured by micro-sawing technology (Jang et al. 2003)

1.2.2 Modern Technology

1.2.2.1 MEMS (Micro-Electro-Mechanical Systems)

Much of the current research in MEMS centers on a group of batch micro-fabrication methods that arose from the semiconductor sector. Many technologies are included among MEMS methods: wet etching, dry etching, LIGA (Lithographie, Galvanoformung, and Abformung), and deep reactive ion etching (DRIE). This section will focus on DRIE technology, which is the most widely used among MEMS technologies. As shown in Table 1.1, rectangular, circular, triangular, or trapezoidal channels can be fabricated using the DRIE technique. This technology is applicable to metal, silicon, and glass with a wide range of channel sizes, from the nanometer scale to the millimeter scale. In addition, the technology has the advantage of low manufacturing uncertainty. However, the DRIE technology is not well suited for use in industrial fields due to its time-consuming process.

The DRIE technology process shown in Fig. 1.6 is as follows: (1) Deposit Photo Resistor (PR) material on the specimen using a sputtering process; (2)

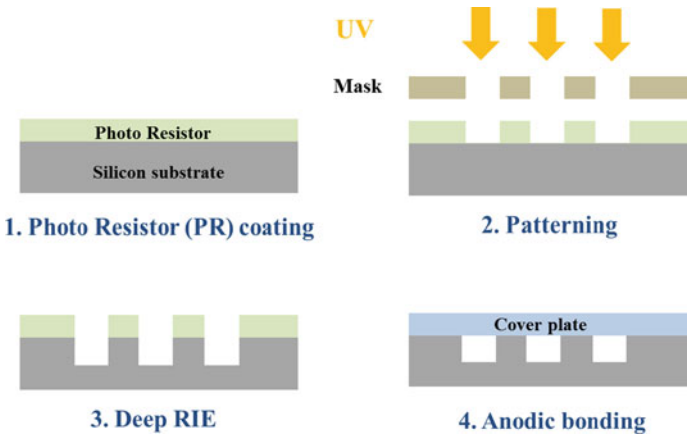

Fig. 1.6 Process of DRIE technology (Youn and Kim 2012)

Expose the specimen to UV light; (3) Form the channels by the DRIE process; (4) Join a cover with the specimen by anodic bonding.

1.2.2.2 Laser Micro-Machining

Recently, laser micro-machining technology has been applied to the fabrication of microchannels. Laser micro-machining is applicable to any material and can produce a wide range of channel sizes from the nanometer to millimeter scale in an unlimited number of geometries. In addition, the technology has the advantage of low manufacturing uncertainty. Laser micro-machining technology is better than the technologies discussed above in all aspects except cost and process speed. For this reason, the technique has not yet been adopted by industry. A diagram of a laser micro-machining system is shown in Fig. 1.7a. The laser enters a test section through a focusing lens while a computer-controlled XYZ-stage moves the specimen to form the microchannels. Figure 1.7b and c shows some microchannels manufactured by the laser micro-machining process.

1.3 Single-Phase Flow in Microchannels

Many experimental correlations for pressure drop have been developed from experimental measurements. Since the pioneering work done by Tuckerman and Pease (1981) for high heat flux removal by microchannel arrays, much of the research has concentrated on fluid flow paths having constant cross-section. In 1981, Tuckerman and Pease investigated the ability of microchannels to cool integrated circuits. They reported that water-cooled microchannels fabricated on

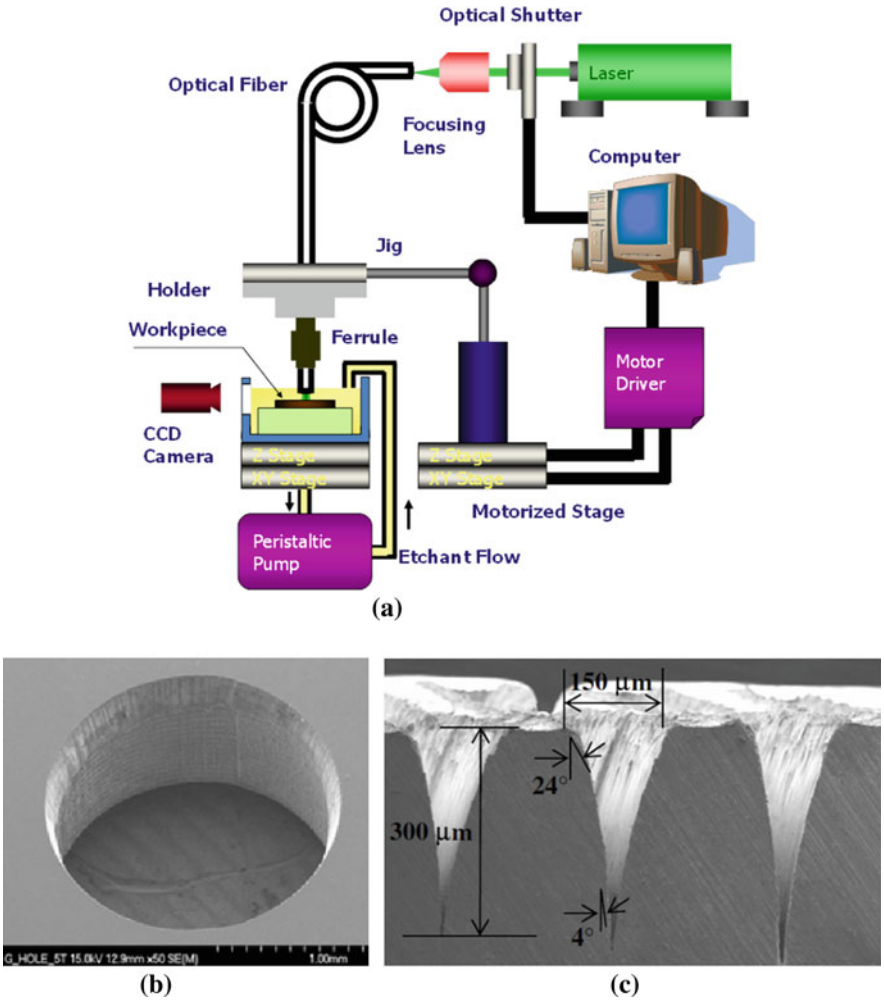

Fig. 1.7 **a** Schematic diagram of a laser micro-machining system; **b** Drilling of 1 μm-thick glass with hole diameter of 1 μm; **c** A scanning electron microscope image of the cross-section of microchannels fabricated using femtosecond laser micro-machining (Lim et al. 2008)

the substrate of the IC chip could dissipate heat of 790 W/cm^2 without a phase change and with maximum substrate temperature rise of 71 °C above the inlet water temperature. Shortly after Tuckerman and Pease, Wu and Little (1983, 1984) conducted several experiments with gas flowing instead of liquid in the trapezoidal-shaped silicon/glass microchannel to measure the flow friction and heat transfer characteristics. They reported that the transition from laminar to turbulent flow occurs at Reynolds numbers of 400–900 depending on test conditions. They suggested that reducing the transition Reynolds number improved the heat transfer.

Pfahler et al. (1990) experimentally investigated three microchannels of rectangular cross-section ranging in the area 80–7200 μm^2 using N-propanol as the working fluid and reported the result of fluid flow and friction factor. Their target was to determine at what length the continuum equation broke down. Later, they (Pfahler et al. 1991) continued a series of experiments to measure friction factors using liquids and gases in microchannels. Peng and Wang (1993), Wang and Peng (1994), Peng et al. (1995), and Peng and Peterson (1996) performed studies on heat transfer and fluid flow for different microchannnels and microchannel structures. They tested for water and methanol in microchannels with hydraulic diameters ranging from 0.3 to 0.75 mm and obtained the laminar/turbulent transition in the Reynolds number range of 700–1100. Yu et al. (1995) presented results for the flow of nitrogen gas and water in microtubes with diameters of 19, 52, and 102 μm. In laminar flow, the transition from laminar to turbulent occurred in the range of $2000 < \mathrm{Re} < 6000$.

Hwang and Kim (2006) investigated the pressure drop characteristics in microtubes with inner diameter of 0.244, 0.430, and 0.792 mm using R-134a as a test fluid in the Reynolds number range of 150–10,000. Yen et al. (2003) performed an experimental investigation in microtubes of 0.19, 0.30, and 0.51 mm using HCFC123 and FC-72 as the working fluids and reported the results of fluid flow and heat transfer. They showed that the friction factor in microtubes is well matched with its analytical laminar flow value in the Reynolds number range 20–265. Xu et al. (2000) investigated water flow in microchannels both experimentally and analytically, with Reynolds numbers ranging from 20 to 4000 and hydraulic diameters from 30 to 344 μm.

1.3.1 Pressure Drop Correlations

The following equations are readily derived based on the continuum assumption for Newtonian liquid flows in a smooth circular pipe. Considering the equilibrium of a fluid element of length dx in a pipe of diameter d, the force due to pressure difference dp is balanced by the frictional force due to shear stress τ_w at the wall:

$$\left(\frac{\pi}{4}d^2\right)\mathrm{d}p = (\pi \mathrm{d}\,\mathrm{d}x)\tau_w \tag{1.1}$$

The pressure gradient and the wall shear stress are thus related by the following equation:

$$\frac{\mathrm{d}p}{\mathrm{d}x} = \frac{4\tau_w}{d} \tag{1.2}$$

For Newtonian fluids, the wall shear stress τ_w is expressed in terms of the velocity gradient at the wall:

$$\tau_w = \mu \left. \frac{du}{dy} \right|_w \tag{1.3}$$

where μ is the viscosity of fluid. The friction factor f is thus related by the following equation:

$$f = \frac{\tau_w}{(1/2)\rho u_m^2} \tag{1.4}$$

where u_m is the mean flow velocity in the channel.

The frictional pressure drop p over a length L is obtained from Eqs. (1.2) and (1.4):

$$\Delta p = \frac{2f\rho u_m^2 L}{d} \tag{1.5}$$

For non-circular flow channels, the d in Eq. (1.5) is replaced by the hydraulic diameter d_h represented by the following equation:

$$d_h = \frac{4A_c}{P_w} \tag{1.6}$$

where A_c is the flow-channel cross-sectional area and P_w is the wetted perimeter. For a rectangular channel of sides a and b, d_h is given by

$$d_h = \frac{4ab}{2(a+b)} \tag{1.7}$$

The friction factor f in Eq. (1.5) depends on the flow conditions. The following relation for the friction factor of a laminar flow is theoretically given as

$$f = \frac{64}{\mathrm{Re}} \tag{1.8}$$

where the constant 64 is changed by the geometry of the channel cross-section. Table 1.2 shows the list of values of the constant (called the Poiseuille number) for different geometries. As shown in Fig. 1.8, Eq. (1.8) is well matched with the experimental data of Yen et al. (2003) for the microchannels of 0.19 and 0.51 mm.

For turbulent flows many types of relations are available in the literature for friction factor. These are generally defined by the Blasius equation as

$$f = 0.316\mathrm{Re}^{-1/4} \tag{1.9}$$

As shown in Fig. 1.9, Eq. (1.9) is well matched with the experimental data of Hwang and Kim (2006) for the microchannels of 0.244, 0.43, and 0.792 mm.

Table 1.2 Characteristic values of laminar flow in circular and noncircular channels (Celata 2004)

Channel cross section	Channel geometry	Hydraulic diameter	Constant
Circle	diameter d	d_h	64
Rectangular	a, b, a/b = 0.1	2ab/(a + b)	85.76
Rectangular	a, b, a/b = 0.2	2ab/(a + b)	76.8
Rectangular	a, b, a/b = 0.4	2ab/(a + b)	65.28
Rectangular	a, b, a/b = 0.6	2ab/(a + b)	60.16
Rectangular	a, b, a/b = 0.8	2ab/(a + b)	57.6
Square	Side a	a	56.96

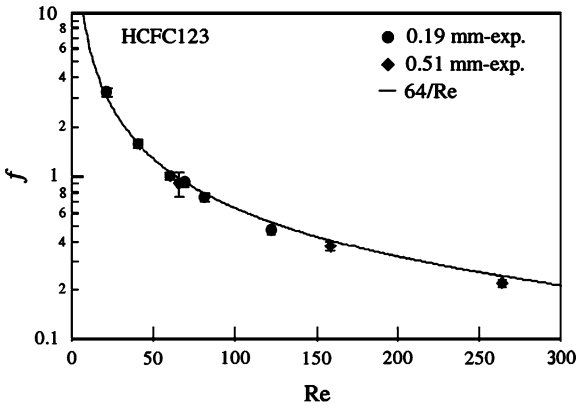

Fig. 1.8 Comparison between the frictional factor of turbulent flow and the experimental results of Yen et al. (2003)

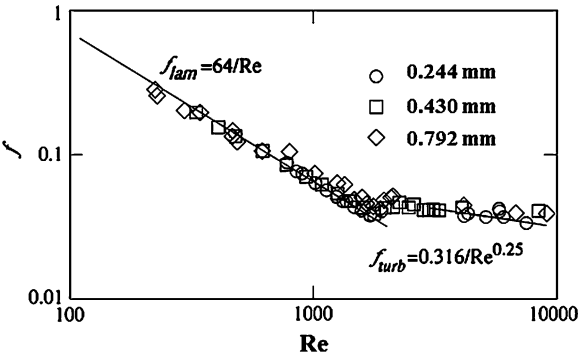

Fig. 1.9 Comparison between the frictional factor of turbulent flow and the experimental results of Hwang and Kim (2006)

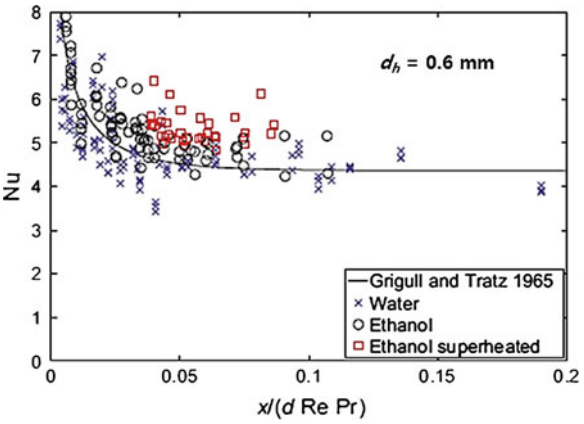

Fig. 1.10 Nusselt number as a function of dimensionless length and experimental results compared with Eq. (1.10) (Shilder et al. 2010)

1.3.2 Heat Transfer Correlations

1.3.2.1 Laminar Flow

The Nusselt number of a fully developed laminar flow is 4.36 when there is a constant heat flux boundary condition at the tube wall is a constant heat flux. Grigull and Tratz (1965) numerically investigated the thermal entrance problem for laminar flow with constant heat flux. They evaluated the Nusselt number as a function of the dimensionless axial distance, Reynolds number, and Prandtl number:

$$Nu = 4.36 + \frac{0.00668(d_h/x)\mathrm{Re\ Pr}}{1 + 0.04[(d_h/x)\mathrm{Re\,Pr}]^{2/3}} \tag{1.10}$$

Shilder et al. (2010) conducted an experiment for single phase flow in a microchannel that had a hydraulic diameter of 0.6 mm. If the experimental uncertainties are accounted for, as shown in Fig. 1.10, the measurements by Shilder et al. (2010) agree with the classical theory of Eq. (1.10).

1.3.2.2 Turbulent Flow

Adams et al. (1997) conducted experimental work in the turbulent region with water flow in circular microchannels of 0.76 and 0.109 mm. Based on their data, they proposed the following equation:

$$\mathrm{Nu} = \mathrm{Nu}_{Gn}(1 + F) \tag{1.11}$$

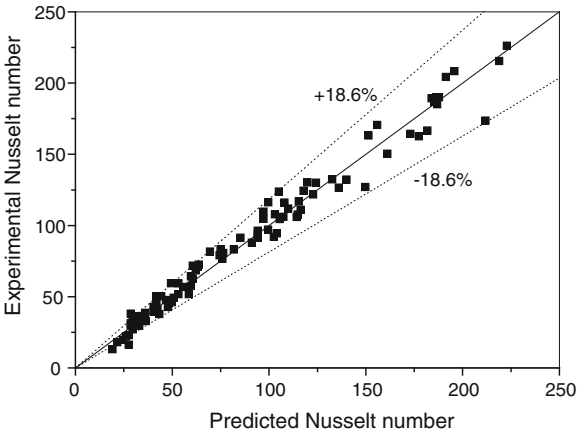

Fig. 1.11 Comparison between the experimental results of Yu et al. (1995) and the correlation proposed by Adams et al. (1997)

where

$$\mathrm{Nu}_{Gn} = \frac{(f/8)(\mathrm{Re} - 1000)\,\mathrm{Pr}}{1 + 12.7(f/8)^{1/2}(\mathrm{Pr}^{2/3} - 1)} \tag{1.12}$$

$$f = (1.82\log(\mathrm{Re}) - 1.64)^{-2} \tag{1.13}$$

$$F = 7.6 \times 10^{-5}\mathrm{Re}\left(1 - (d_h/d_o)^2\right) \tag{1.14}$$

Nu_{Gn} represents the Nusselt number predicted by Gnielinski's (1976) correlation. The least-squares fit to all the data sets studied by Adams et al. (1997) resulted in $d_o = 1.164$ mm. As shown in Fig. 1.11, the correlations are well matched with the experimental data for the 0.102, 0.76, and 1.09 mm microchannels of Yu et al. (1995), within ±18.6 %.

1.4 Phase-Change (multi-phase) Flow in Microchannels

1.4.1 Pressure Drop Correlations

Many investigations have examined the pressure drop correlations for two-phase flow (Ghiaasiaan, 2008). Lockhart and Martinelli (1949) defined a two-phase friction multiplier to relate the two-phase pressure gradient to the single-phase pressure gradient for liquid flow:

$$\left(\frac{\mathrm{d}P}{\mathrm{d}z}\right)_{TP} = \left(\frac{\mathrm{d}P}{\mathrm{d}z}\right)_{L} \Phi_L^2 \tag{1.15}$$

Table 1.3 Constant and exponents in the correlation of Lee and Lee (2001)

Liquid regime	Gas flow regime	A	q	r	s
Laminar	Laminar	6.833×10^{-8}	−1.317	0.719	0.577
Laminar	Turbulent	6.185×10^{-2}	0	0	0.726
Turbulent	Laminar	3.627	0	0	0.174
Turbulent	Turbulent	0.408	0	0	0.451

The friction multiplier, Φ_L^2, is defined by coefficient C and the Lockhart-Martinelli parameter, X^2, as the ratio of the single-phase liquid and gas pressure gradients.

$$\Phi_L^2 = 1 + \frac{C}{X} + \frac{1}{X^2} \tag{1.16}$$

$$X = \sqrt{\frac{(\mathrm{d}P/\mathrm{d}z)_L}{(\mathrm{d}P/\mathrm{d}z)_G}} \tag{1.17}$$

Chisholm and Laird (1958) related the friction multiplier to the Lockhart-Martinelli parameter through a simple expression that depends on the coefficient C ranging from 5 to 20, depending on laminar or turbulent flow of gas and liquid. Some researchers have suggested empirical correlations for the coefficient C to determine the two-phase friction multiplier. Among the suggested correlations, the most widely used correlations are Mishima and Hibiki's correlation (1996) and Lee and Lee's correlation (2001). Mishima and Hibiki's correlation appears to provide the best correlation for adiabatic two-phase flow, although its applicability to minichannel flows with phase change has not been demonstrated. They have proposed

$$C = 21(1 - e^{-0.319 d_h}) \tag{1.18}$$

where the diameter d_h is in millimeters. Cavallini et al. (2005) have recently shown that Mishima and Hibiki's method can predict the two-phase pressure drop for flow condensation of refrigerants R-134a and R-236ea in 1.4 mm tubes. The correlation of Mishima and Hibiki (1996) evidently assumes that C depends on channel size only. Based on the observation that C depends on phase mass fluxes as well, and using experimental data from several sources as well as their own data that covered channel gaps in the 0.4 to 4 mm range, Lee and Lee (2001) derived the following correlation for C, for adiabatic flow in horizontal thin rectangular channels:

$$C = A\left(\frac{\mu_L^2}{\rho_L \sigma d_h}\right)^q \left(\frac{\mu_L j}{\sigma}\right)^r \mathrm{Re}_{L0}^s \tag{1.19}$$

where j represents the total mixture volumetric flux. The constants A, r, q, and s depend on the liquid and gas flow regimes (viscous or turbulent), and their values are listed in Table 1.3.

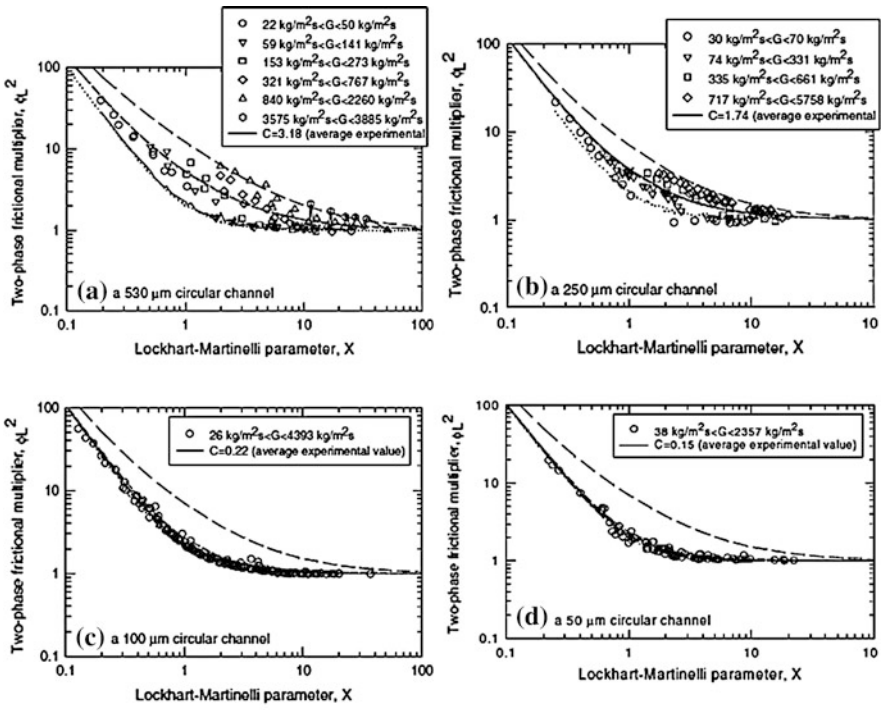

Fig. 1.12 Pressure drop characteristics of two-phase flow: Variation of the two-phase multiplier with the Lockhart-Martinelli parameter (Chung and Kawaji 2004)

The correlations of Mishima and Hibiki (1996) and Lee and Lee (2001), Eqs. (1.18) and (1.19), respectively, predicted the data of Chung et al. (2004) for adiabatic flow of water and nitrogen in horizontal 96 μm square rectangular microchannels, the data of Zhao and Bi (2001) for water and air flow in a miniature triangular channel with $d_h = 0.87–2.89$ mm, and the data of Chung and Kawaji (2004) for water and nitrogen flow in a horizontal circular channel with $d_h = 50–530$ μm, within about 10 % accuracy. Figure 1.12 shows the two-phase friction multiplier data plotted against the Lockhart-Martinelli parameter for the data of Chung and Kawaji (2004).

1.4.2 Heat Transfer Correlations

A sequence of two-phase and boiling heat transfer regimes takes place along the heated channels during flow boiling. The sequence of flow regimes includes bubbly, slug, churn, and annular flow. Following the initiation of boiling, the

sequence of heat transfer regimes includes subcooled boiling, saturated nucleate boiling, saturated forced-flow boiling, and dry out field. Among the heat transfer regimes observed in flow boiling, the most commonly observed regime is the saturated flow boiling regime, which will be the focus of this section. Saturated, forced-flow boiling refers to the entire region between the point where $x = 0$ and the critical heat flux point. A sequence of complicated two-phase flow patterns, including bubbly, churn, slug, and annular-dispersed, can take place. The two-phase flow regimes cover a quality range of a few percent, up to very high values characteristic of annular flow regime (sometimes approaching 100 %). Nucleate boiling is predominant where quality is low (a few percent); forced convective evaporation is predominant at high qualities representing annular flow; and elsewhere both mechanisms can be important. The relative contribution of forced convection increases as quality increases.

Nucleate boiling and forced convective evaporation both contribute to the heat transfer in saturated flow boiling. At low x, the contribution of the nucleate boiling mechanism dominates, but the contribution of convection increases as quality is increased. Once the annular-dispersed flow regime is achieved, the contribution of convective evaporation becomes predominant. Forced-flow boiling correlations should thus take into account the composite nature of the boiling heat transfer mechanism. Correlations for saturated flow boiling are reviewed next.

1.4.2.1 Chen's Correlation (1966)

Chen's correlation is among the oldest, most successful and widely used correlations for saturated boiling. It works well for water at relatively low pressure and has been applied to a variety of fluids. The correlation can be used for $d_h \geq 1$ mm, $P = 0.09$–3.45 Mpa, $x = 0$–0.7, $q'' = 0$–2.4 MW/m^2.

$$h = h_{NB} + h_{FC} \tag{1.20}$$

The forced convection component is found from

$$h_{FC} = 0.023 \mathrm{Re}_f^{0.8} \mathrm{Pr}_f^{0.4} F \left(\frac{k_f}{d_h} \right) \tag{1.21}$$

where

$$\mathrm{Re}_f = G(1 - x) d_h / \mu_f \tag{1.22}$$

$$\mathrm{Pr}_f = (\mu C_p / k)_f \tag{1.23}$$

The factor F represents $(\mathrm{Re_{TP}}/\mathrm{Re}_f)^{0.8}$ and was correlated by Chen empirically in a graphical form. A curve fit to the graphical correlation is (Collier 1981):

$$F = \begin{cases} 1 & \text{for } X_u^{-1} < 0.1 \\ 2.35(0.213 + X_u^{-1})^{0.736} & \text{for } X_u^{-1} > 0.1 \end{cases} \tag{1.24}$$

The nucleate boiling component is based on the correlation of Forster and Zuber (1955), modified to account for the reduced average superheat in the thermal boundary layer on bubble nucleation on wall cavities:

$$h_{NB} = 0.00122 \left\{ \frac{k_f^{0.79} C_{pf}^{0.45} \rho_f^{0.49} g_c^{0.43}}{\sigma^{0.5} \mu_f^{0.29} h_{fg}^{0.24} \rho_g^{0.24}} \right\} \Delta T_{sat}^{0.24} \Delta P_{sat}^{0.75} S \tag{1.25}$$

where $\Delta T_{sat} = T_w - T_{sat}$ and $\Delta P_{sat} = P_{sat}(T_W) - P$. Note that g_c is needed for English units only. The parameter S is Chen's suppression factor and represents $S = (\Delta T_{\text{eff}}/\Delta T_{\text{sat}})^{0.99}$, where ΔT_{eff} is the effective liquid superheat in the thermal boundary layer. S was also correlated graphically. An empirical curve fit to Chen's graphical correlation is (Collier 1981):

$$S = \left[1 + (2.56 \times 10^{-6})(\text{Re}_f F^{1.25})^{1.17} \right]^{-1} \tag{1.26}$$

1.4.2.2 Kandlikar's Correlation (1990)

Kandlikar's correlation is based on 10,000 data points for water, refrigerants and cryogenic fluids. The correlation can be used for $d_h \geq 1$ mm.

$$h = \max(h_{NBD}, h_{CBD}) \tag{1.27}$$

$$h_{CBD} = \left\{ 1.136\text{Co}^{-0.9}(1-x)^{0.8} f_2(\text{Fr}_{\text{f0}}) + 667.2\text{Bl}^{0.7}(1-x)^{0.8} F_{fl} \right\} h_{\text{f0}} \tag{1.28}$$

$$h_{NBD} = \left\{ 0.6683\text{Co}^{-0.2}(1-x)^{0.8} f_2(\text{Fr}_{\text{f0}}) + 1058\text{Bl}^{0.7}(1-x)^{0.8} F_{fl} \right\} h_{\text{f0}} \tag{1.29}$$

where

$$h_{\text{f0}} = \frac{k_f}{d_h} \frac{(\text{Re}_f - 1,000)(f/2)\,\text{Pr}_f}{[1 + 12.7(\text{Pr}_f^{2/3} - 1)(f/2)^{0.5}]} \tag{1.30}$$

The parameters in Kandlikar's correlation are the convection number Co, the boiling number Bl, and the Froude number when all mixture is saturated liquid, Fr_{f0}, defined, respectively, as

$$\text{Co} = (\rho_g/\rho_f)^{0.5}[(1-x)/x]^{0.8} \tag{1.31}$$

$$\text{Bl} = q''_w/(Gh_{fg}) \tag{1.32}$$

Table 1.4 Values of the fluid-surface parameter F_{fl} in the correlation of Kandlikar (1997)

Fluid	F_{fl}	Fluid	F_{fl}
Water	1.00	R-32/R-1132	3.30
R-11	1.30	R-124	1.00
R-12	1.50	R-141b	1.80
R-13BI	1.31	R-134a	1.63
R-22	2.20	R-152a	1.10
R-113	1.30	Kerosene	0.488
R-114	1.24	Nitrogen	4.70
		Neon	3.50

Note Use 1.0 for any fluid with a stainless steel tube

and

$$\mathrm{Fr}_{\mathrm{f0}} = G^2/(\rho_f^2 g d_h) \tag{1.33}$$

The parameter F_{fl} is the fluid-surface parameter discussed above (see Table 1.4). Finally,

$$f_2(\mathrm{Fr}_{\mathrm{f0}}) = \begin{cases} 1 & \text{for } \mathrm{Fr}_{\mathrm{f0}} \geq 0.4 \\ (25\mathrm{Fr}_{\mathrm{f0}})^{0.3} & \text{for } \mathrm{Fr}_{\mathrm{f0}} < 0.4 \end{cases} \tag{1.34}$$

1.4.2.3 Gungor and Winterton's Correlation (1986)

Gungor and Winterton's correlation is based on 3,700 data points for water, refrigerants, and ethylene glycol. The correlation can be used for $d_h \geq 1$ mm. The original correlation (Gungor and Winterton 1986) was subsequently simplified by the authors (Gungor and Winterton 1987) to the following easy-to-use correlation:

$$h = h_f\left\{1 + 3000\mathrm{Bl}^{0.86} + 1.12[x/(1-x)]^{0.75}[\rho_f/\rho_g]^{0.41}\right\}E_2 \tag{1.35}$$

where

$$E_2 = \begin{cases} 1 & \text{for } \mathrm{Fr}_{\mathrm{f0}} \geq 0.05 \\ \mathrm{Fr}_{\mathrm{f0}}^{(0.1-2\mathrm{Fr}_{\mathrm{f0}})} & \text{for } \mathrm{Fr}_{\mathrm{f0}} < 0.05 \end{cases} \tag{1.36}$$

1.4.2.4 Shah's Correlation (1982)

Shah (1982) proposed correlations to implement his chart calculation method and recent comparisons show his correlations perform satisfactorily for mini- and macrochanenls. Shah's correlations consider nucleate and convective boiling both to be important to the two-phase flow evaporative heat transfer. Similar to Chen

(1966), his method chooses the larger of the two as the dominant contributor to the local two-phase flow boiling heat transfer coefficient. Shah's method is meant to be applicable to both vertical and horizontal tubes.

When $N > 1.0$ and $\mathrm{Bl} > 0.0003$, h is calculated as below:

$$h = 230\mathrm{Bl}^{0.5} h_f \tag{1.37}$$

where

$$N = \left(\frac{1-x}{x}\right)^{0.8} \left(\frac{\rho_g}{\rho_f}\right)^{0.5} \tag{1.38}$$

When $N > 1.0$ and $\mathrm{Bl} < 0.0003$, h is calculated as below:

$$h = \left(1 + 46\mathrm{Bl}^{0.5}\right) h_f \tag{1.39}$$

When $1.0 > N > 0.1$, h is calculated as below:

$$h = F_s \mathrm{Bl}^{0.5} \exp(2.74N - 0.1) h_f \tag{1.40}$$

When $N < 0.1$, h in the bubble suppression regime is calculated using the equation below:

$$h = F_s \mathrm{Bl}^{0.5} \exp(2.74N - 0.15) h_f \tag{1.41}$$

In the above equations, Shah's constant $F_s = 14.7$ when $\mathrm{Bl} > 0.0011$ and $F_s = 15.43$ when $\mathrm{Bl} < 0.0011$. Shah (2006) compared several correlations for conventional channels against a wide range of data that included 30 pure fluids. Best results were found with the correlations of Shah (1982) and Gungor and Winterton (1987), the mean deviation for all data being about 17 %.

1.4.2.5 Li and Wu's Correlation (2010)

Recently, Li and Wu obtained a correlation using the boiling number, Bond number, and Reynolds number. The correlation contains more than 3,744 data points, covering a wide range of working fluids, operational conditions, and different microchannel dimensions. In addition, they showed that the Bond number in predicting heat transfer coefficients can be used as a criterion to classify a flow path as a microchannel or as a conventional macrochannel. The correlation can be used for 0.19 mm $\leq d_h \leq$ 2.01 mm.

$$h = 334\mathrm{Bl}^{0.3} \left(\mathrm{Bo}Re_f^{0.36}\right)^{0.4} (k_f/d_h) \tag{1.42}$$

where

$$\mathrm{Bl} = q''_w/(Gh_{fg}) \tag{1.43}$$

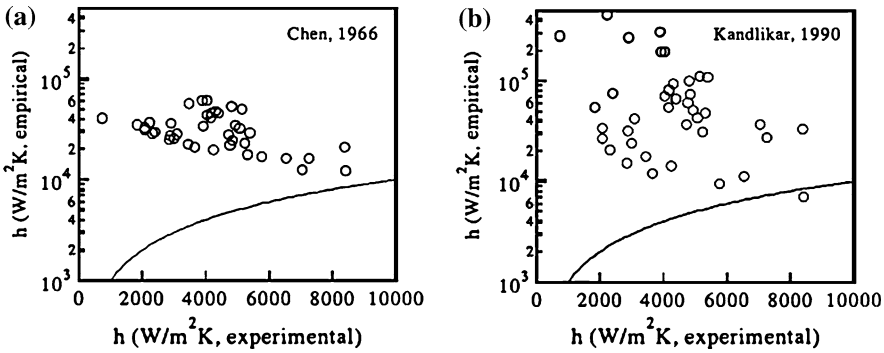

Fig. 1.13 Comparison between the experimental results of Yen et al. (2003) and **a** the correlation proposed by Chen (1996), and **b** the correlation proposed by Kandlikar (1990)

$$\mathrm{Bo} = \frac{g(\rho_l - \rho_g)d_h^2}{\sigma} \tag{1.44}$$

1.5 Comparison of the Selected Correlations

The correlations by Chen, Kandlikar, and Gungor and Winterton predict experimental data well for cases where the channel hydraulic diameter is larger than 0.5 mm. However, recent studies by Yen et al. (2003) and Li and Wu (2010) show that the correlations by Chen, Kandlikar, and Gungor and Winterton over-predict or under-predict the experimental data of microchannels. As shown in Fig. 1.13, Chen's correlation and Kandikar's correlation under-predicted the experimental data of Yen et al. (2003) by more than an order of magnitude. In addition, as shown in Fig. 1.14, Gungor and Winterton's correlation over-predicted the experimental data for channels having hydraulic diameters of 0.586 and 0.19 mm, while the correlation was well matched with the data for the 2.01 mm channel. However, Li and Wu's correlation predicted the experimental data well for the range of hydraulic diameters from 0.19 to 2.01 mm.

1.5.1 Two-Phase Flow Correlations Without Phase Change

Gas–liquid flows have been studied extensively due to their presence in nature and usefulness in many important industrial applications including oil transport, steam generation, bubble columns, reactors, aeration systems for chemical processes, and cooling systems for energy production. More recently, two-phase flows within microchannels have been receiving attention because of their applicability to such fields as MEMS, electronics cooling, medical and genetic engineering, and

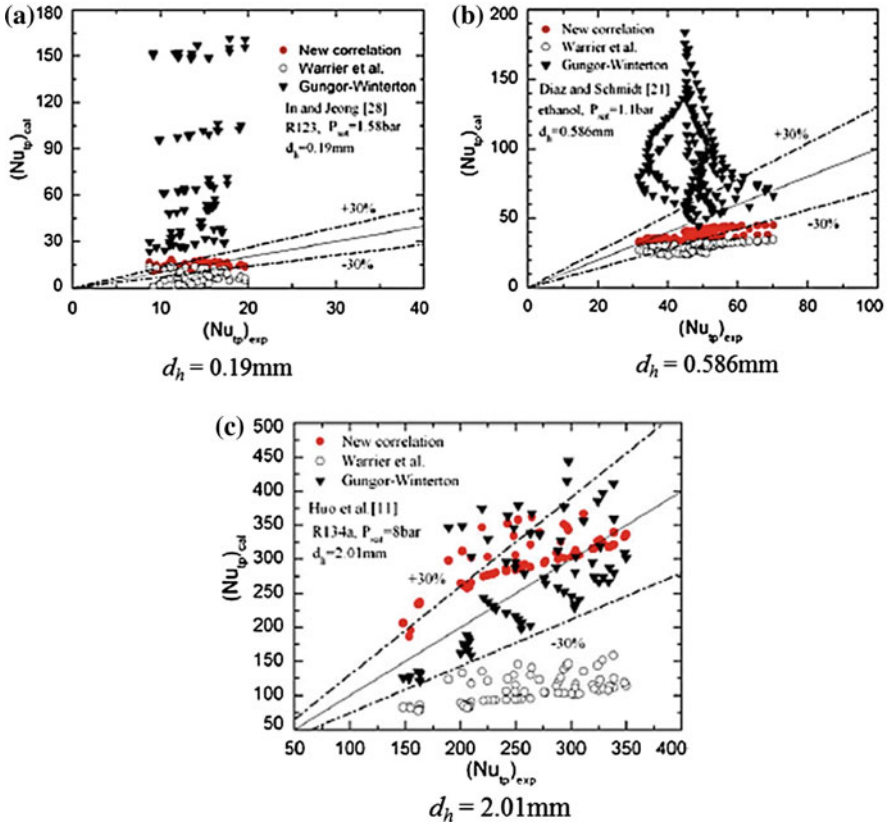

Fig. 1.14 Comparison between the experimental results and the correlations: **a** $d_h = 0.19$ mm; **b** $d_h = 0.586$ mm; and **c** $d_h = 2.01$ mm (Li and Wu 2011)

bioengineering. To design and evaluate the performance of devices in these fields, investigators must have fundamental knowledge of two-phase flow characteristics in small flow passages, including flow pattern, void fraction, pressure drop, and heat transfer coefficient.

Many studies have been conducted on the flow and heat transfer characteristics of two-phase flows within microchannels because of their practical applications. The majority of research on two-phase flow has focused on configurations in which flow boiling arises, and thus many flow boiling heat transfer characteristics and empirical correlations have been presented (Schilder et al. 2010; Morini 2004; Lelea et al. 2004; Celata et al. 1993; Choo and Kim 2010a). In addition, many researchers have observed flow patterns in microchannels and presented flow pattern maps for the purpose of understanding the relationship between heat transfer and flow characteristics (Serizawa et al. 2002; Chung and Kawaji 2004; Triplett et al. 1999).

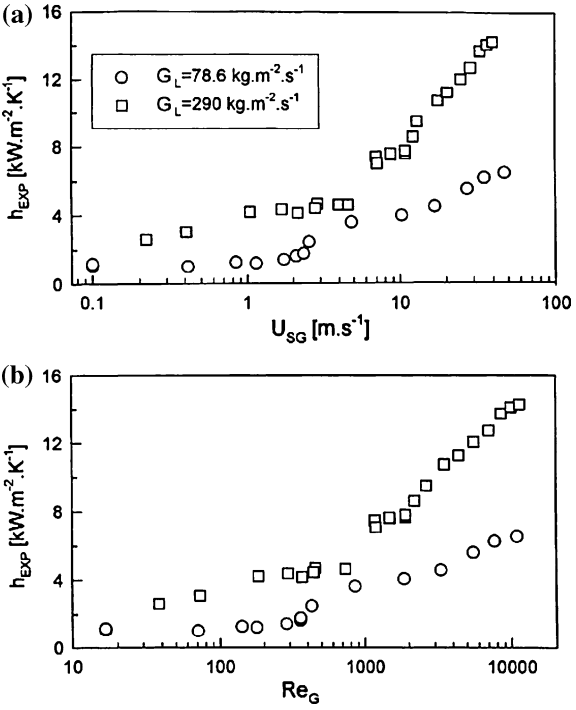

Fig. 1.15 A plot of the experimentally determined heat transfer coefficient as a function of the superficial gas velocity and the gas Reynolds number (Hetsroni et al. 2009)

Recently, heat transfer experiments were conducted by Bao et al. (2000) using a 1.95 mm diameter minichannel under non-boiling, air–water flow conditions. The results of this research showed that heat transfer performance increased with increasing air flow rate at a fixed liquid flow rate. Flow patterns were not observed as a part of this work, but the investigators suggested that the augmentation in heat transfer was caused by the transition of the flow regime from bubbly to intermittent slug to annular. Hetsroni et al. (2009) conducted research using a 0.1 mm microchannel using an air–water flow under non-boiling conditions. The microchannel was manufactured onto a silicon substrate using a MEMS process. They observed decreasing heat transfer performance as the air flow rate was increased under fixed water flow rate conditions. The heat transfer results for microchannels of Hetsroni et al. (2009) showed opposite trends from those for minichannels of Bao et al. (2000). Therefore, it is expected that there exists a transition diameter that distinguishes the heat transfer characteristics of microchannels from minichannels. Finally, Choo and Kim (2011) showed the transition diameter that distinguishes the heat transfer characteristics of microchannels from minichannels.

Bao et al. (2000) studied a 1.95 mm diameter minichannel under non-boiling, air–water flow conditions. Figure 1.15 shows the experimental heat transfer coefficients for horizontal flows with (a) a liquid mass flux of 78.6 kg $m^{-2}s^{-1}$ and a heat flux of 20 kW m^{-2}, and (b) a liquid mass flux of 290 kg $m^{-2}s^{-1}$ and a heat flux of 33 kW m^{-2} plotted against the gas superficial velocity and plotted against

the gas-phase Reynolds number at the heating section. As expected, the heat transfer coefficient increases with increasing liquid mass flux and increasing gas superficial velocity or Reynolds number. The data show a sharp increase in the heat transfer coefficient at a gas velocity of about 3 m/s and a gas superficial velocity of 5.5 ms^{-1}. The measured heat transfer coefficients for the air–water system are always higher than would be expected for the corresponding single-phase liquid flow, so the addition of air can be considered to have an enhancing effect. This effect presumably arises from the increased liquid velocity caused by the presence of the gas phase and from higher turbulence intensities due to the relative motion between the phases.

Hetsroni et al. (2009) conducted research using a 0.1 mm microchannel using air–water flow under non-boiling conditions. The microchannel was manufactured onto a silicon substrate using a MEMS process. With increasing superficial gas velocity, a gas core with a thin liquid film was observed. The visual observation showed that as the air velocity increased, the liquid droplets entrained in the gas core disappeared such that the flow became annular. The probability of appearance of different flow patterns should be taken into account for developing flow pattern maps. The dependence of the Nusselt number on liquid and gas Reynolds numbers, based on liquid and gas superficial velocity, respectively, was determined to be in the range of $\mathrm{Re}_{LS} = 4$–56 and $\mathrm{Re}_{GS} = 4.7$–270. It was shown that an increase in the superficial liquid velocity involves an increase in heat transfer. This effect was reduced with increasing superficial gas velocity, in contrast to the results reported on two-phase heat transfer in conventional size channels.

The two-phase flow was achieved by introducing water and air into a mixer as shown in Fig. 1.16. The experiments were performed in an open loop, and therefore the outlet pressure was close to atmospheric. Two types of pumps were used: a peristaltic pump and a mini gear pump. The test module is shown in Fig. 1.17. It was fabricated by a 15 × 15 mm square-shaped silicon substrate with a thickness of 530 μm, which was covered by a Pyrex cover, 500 μm-thick, which served as both an insulator and a transparent cover through which flow in the microchannels could be observed. The Pyrex cover was anodically bonded to the silicon chip to seal the channels. In the silicon substrate, parallel microchannels were etched, the cross-section of each channel being an isosceles triangle. The angles at the base were 55°. A test module having 21 microchannels with hydraulic diameter of 130 μm was used.

A microscope with an additional camera joint was assembled to connect a high-speed camera to the microscope. A high-speed camera with a maximum frame rate of 10,000 fps was used to visualize the two-phase flow regimes in the microchannels. In the parallel channels having common inlet and outlet collectors, non-uniform distribution of the working fluid occurred. Simultaneous different flow patterns were observed in different parallel microchannels, as were alternate flow patterns in a given microchannel. These patterns are illustrated in Fig. 1.18.

Results presented in Fig. 1.19 show the dependence of the Nusselt number, Nu_L, based on liquid thermal conductivity, and Reynolds number, Re_{GS}, based on superficial gas velocity and kinematic gas viscosity. As shown in Fig. 1.19, an

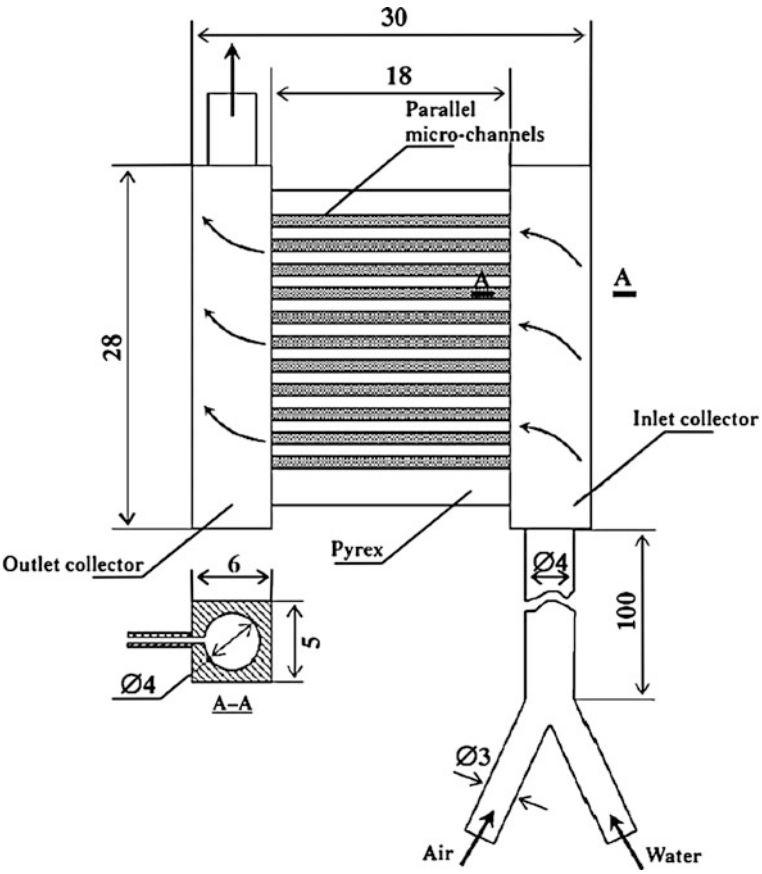

Fig. 1.16 Experimental facility. All dimensions in mm (Hetsroni et al. 2009)

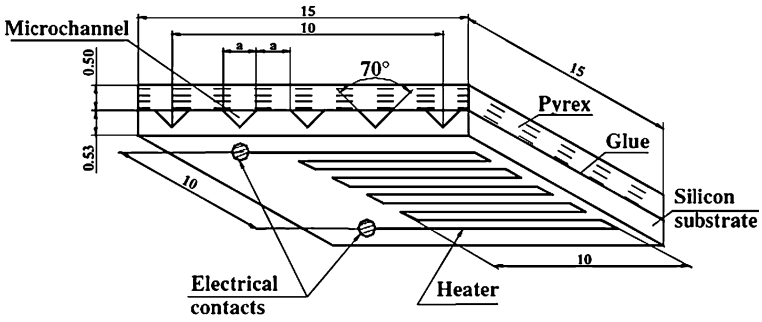

Fig. 1.17 Test module. All dimensions in mm (Hetsroni et al. 2009)

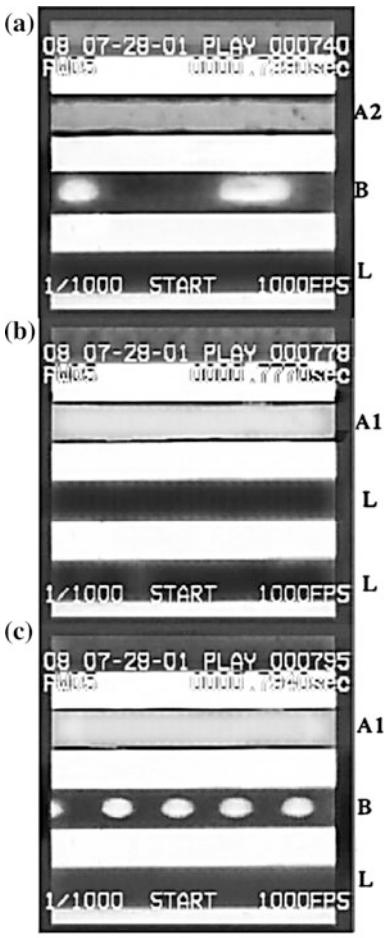

Fig. 1.18 Flow patterns at different times. $U_{GS} = 15$ m/s, $U_{LS} = 0.15$ m/s. **a** t = 0.7320 s, **b** t = 0.7770 s, **c** t = 0.7940 s. L single-phase liquid, B bubbly flow, A1 gas core with thin liquid film; A2, gas core with thick liquid film (Hetsroni et al. 2009)

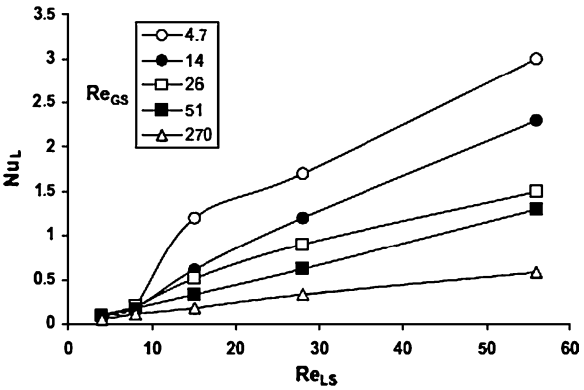

Fig. 1.19 Effect of superficial liquid velocity on heat transfer in parallel triangular microchannels of $d_h = 130$ μm (Hetsroni et al. 2009)

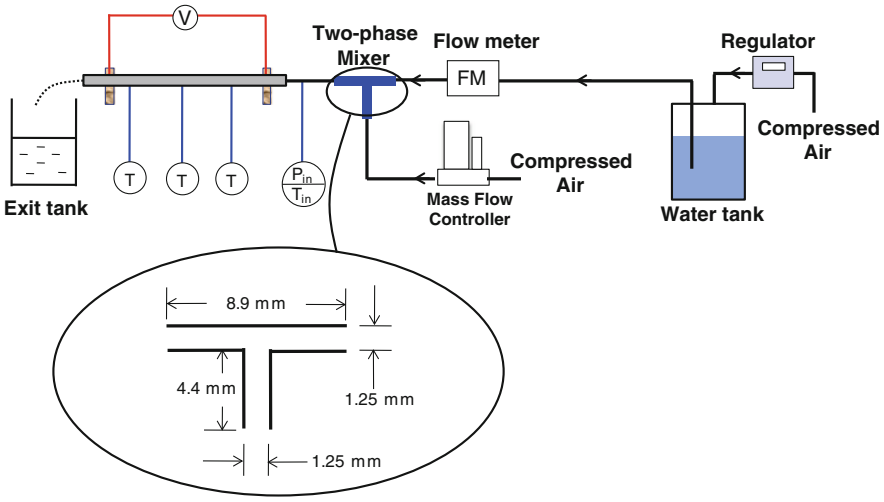

Fig. 1.20 Schematic diagram of experimental setup (Choo and Kim 2011)

increase in superficial liquid velocity leads to an increase in heat transfer. This effect falls off with increasing superficial gas velocity in the range $\mathrm{Re}_{GS} = 4.7$–270. Based on the experimental data, the Nusselt number correlations were developed as shown in Eqs. (1.45) and (1.46).

$$\mathrm{Nu}_L = 0.044\mathrm{Re}_{LS}^{0.96}\mathrm{Re}_{GS}^{-0.18} \quad \text{for} \quad \mathrm{Re}_{GS} = 4.7 - 270,\ \mathrm{Re}_{LS} = 4.0 - 8.0 \tag{1.45}$$

$$\mathrm{Nu}_L = 0.13Re_{LS}^{0.96}\mathrm{Re}_{GS}^{-0.40} \quad \text{for} \quad \mathrm{Re}_{GS} = 4.7 - 270,\ \mathrm{Re}_{LS} = 8.0 - 56 \tag{1.46}$$

Recently, Choo and Kim (2011) obtained the transition diameter that distinguishes the heat transfer characteristics of microchannels from minichannels. They experimentally investigated heat transfer and fluid flow characteristics of non-boiling two-phase flow in microchannels. The effects of channel diameter (140, 222, 334, and 506 μm) on the Nusselt number and the pressure drop were considered. Air and water were used as the test fluids. Results were presented for the Nusselt number and the pressure drop over a wide range of gas superficial velocity (1.24–40.1 m/s), liquid superficial velocity (0.57–2.13 m/s), and wall heat flux (0.34–0.95 MW/m^2). The results showed that the Nusselt number increased with increasing gas flow rate for the large channels of 506 and 334 μm, while the Nusselt number decreased with increasing gas flow for the small channels of 222 and 140 μm. Based on these experimental results, a new correlation for the forced convection Nusselt number was developed. In addition, the two-phase friction multiplier decreased as channel diameter decreased due to the influence of viscous and surface tension forces.

Figure 1.20 shows a schematic diagram of the experimental apparatus. Four circular, stainless steel microchannels with inner diameters of 140, 222, 334, and 506 μm were used in the experiment. The channels were made of stainless steel

Table 1.5 Channel specifications

Channel	D_i (μm)	D_o (μm)	L_{heat} (mm)	L_{total} (mm)
1	506	1580	166	200
2	334	785	150	200
3	222	785	64	100
4	140	785	65	100

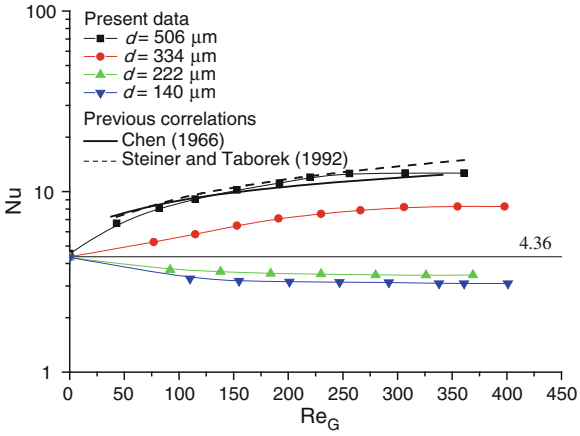

Fig. 1.21 Two-phase Nusselt numbers for each microchannel (Choo and Kim 2011)

304, and the experimental conditions are listed in Table 1.5. Long channels having large length to diameter ratios ($395 \leq L/d \leq 714$) were used to diminish entrance and exit effects. The inner diameter of each microchannel was measured using a scanning electron microscope (SEM). A two-phase mixer was created using a T-junction to mix air and water. At the entrance and exit of the test section, similar T sections were used when measuring pressure and temperature.

The heat transfer characteristics for various air flow rates, at a fixed water flow rate condition, are shown in Fig. 1.21. For the 506 and 334 μm channels, as air flow rate was increased, heat transfer performance increased. This agrees with the results of Bao et al. (2000): the air injected into the minichannel causes turbulent mixing in the liquid film covering the wall. Thus, as the air flow rate is increased, the heat transfer performance increases. This was confirmed through flow pattern observation, as shown in Figs. 1.22 and 1.23. In order to observe the flow patterns, borosilicate glass capillary channels (145, 190, 303, and 506 μm) were used. As shown in Figs. 1.22a and 1.23a, slug and churn flow were observed at low Re_G. Liquid ring flow of churn flow appeared as air flow rate, and thus Re_G increased, as shown in Figs. 1.22b, c and 1.23b, c. A wavy interface was observed between the gas core and liquid film covering the channel wall, caused by turbulence. This agrees with previous observations by Serizawa et al. (2002).

On the other hand, for the 222 and 140 μm channels, at a fixed water flow rate, the heat transfer performance decreased as the air flow rate increased, as shown in

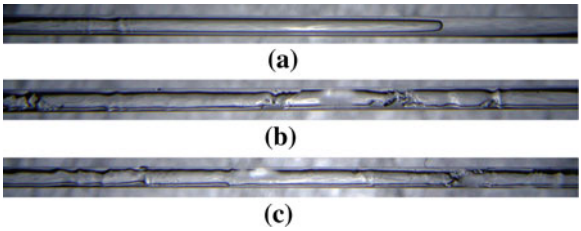

Fig. 1.22 Two-phase flow patterns within 506 μm channel for $Re_L = 420$: **a** $Re_G = 57$; **b** $Re_G = 197$; **c** $Re_G = 370$ V (Choo and Kim 2011)

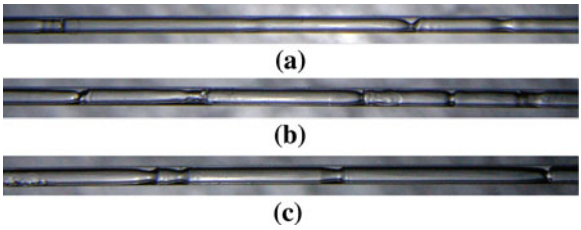

Fig. 1.23 Two-phase flow patterns within 303 μm channel for $Re_L = 420$: **a** $Re_G = 49$; **b** $Re_G = 176$; **c** $Re_G = 354$ (Choo and Kim 2011)

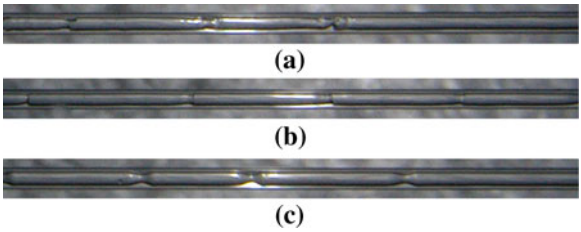

Fig. 1.24 Two-phase flow patterns within 190 μm channel for $Re_L = 420$: **a** $Re_G = 71$; **b** $Re_G = 152$; **c** $Re_G = 333$ (Choo and Kim 2011)

Fig. 1.21. Figures 1.24 and 1.25 show the observed flow patterns for these cases, liquid ring flow only. There was no observable change in the flow pattern over the range of gas-Reynolds numbers investigated. In Figs. 1.24 and 1.25, the turbulent wavy film seen in Figs. 1.22 and 1.23 is absent. The dominant effects of surface tension and liquid viscosity in the 222 and 140 μm channels prohibit turbulence and agitation of the gas–liquid interface, as suggested by Chung and Kawaji (2004), Kandlikar and Grande (2003), and Kawahara et al. (2002). The large asymmetric interfacial waves seen in the 506 and 334 μm channels become thin and axially symmetric in the 222 and 140 μm channels, due to the stronger influence of surface tension on the liquid film structure. That is to say, the separated air and water flow becomes laminar, and the mixing effect disappears, reducing heat transfer. To the best knowledge of the present authors, there is no quantitative information in the open literature on the relationship between heat transfer and the liquid film structure. Further research is required to determine this relationship.

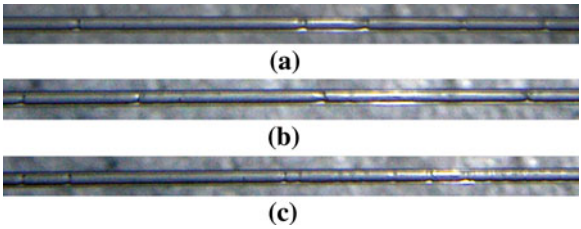

Fig. 1.25 Two-phase flow patterns within 145 μm channel for $Re_L = 420$: **a** $Re_G = 98$; **b** $Re_G = 144$; **c** $Re_G = 321$ (Choo and Kim 2011)

Equation 1.42 below is Chen's correlation (1966) for the two-phase forced convection Nusselt number:

$$Nu_{TP} = 0.023 Re_L^{0.8} Pr_L^{0.4} \left[2.35 \left(0.213 + \frac{1}{X} \right)^{0.736} \right] \tag{1.47}$$

As evaluated by Ghiaasiaan (2008), Chen's correlation is perhaps one of the most widely acknowledged correlation for mini- and microchannels. It works well for water and has been applied to a variety of fluids. In particular, Chen's correlation is known to predict the forced convection contribution to two-phase heat transfer in macroscale channels. However, Chen's correlation does not include change in diameter and, as seen in Fig. 1.21, cannot predict heat transfer characteristics in microchannels that have channel diameters of less than 500 μm. In addition, there is the transition diameter which distinguishes microchannel from minichannel as shown in Fig. 1.26. The slope of the Nusselt number decreases with decreasing channel diameter as shown in Fig. 1.27. Although there are previous correlations of the Nusselt number for forced convection heat transfer (Steiner and Taborek 1992; Gungor and Winterton 1986; Li and Wu 1991; Kandlikar 1990), they cannot predict the heat transfer characteristics of microchannels. The correlations of Steiner and Taborek (1992), Gungor and Winterton (1986), and Liu and Wu (1991) give the Nusselt number as being independent of the channel diameter. Moreover, Kandlikar's correlation (1990) shows that the Nusselt number increases with decreasing the channel diameter. Recently, Choo and Kim (2011) developed a new correlation, as shown below, that accounts for the effect of diameter in two-phase microchannel flow.

$$Nu_{TP} = 0.023 Re_L^m Pr_L^{0.4} F \tag{1.48}$$

where the factor F is meant to represent $(Re_{TP}/Re_L)^m$, given by

$$F = C \cdot X^{-n} \tag{1.49}$$

$$m = 0.8 - 0.8 \left[1 + e^{(d^* - 37)/7} \right]^{-1} \tag{1.50a}$$

$$C = 2.94 + 358 \cdot e^{-(0.1 d^*)} \tag{1.50b}$$

$$n = 0.7 - 0.8 \left[1 + e^{(d^* - 41)/2} \right]^{-1} \tag{1.50c}$$

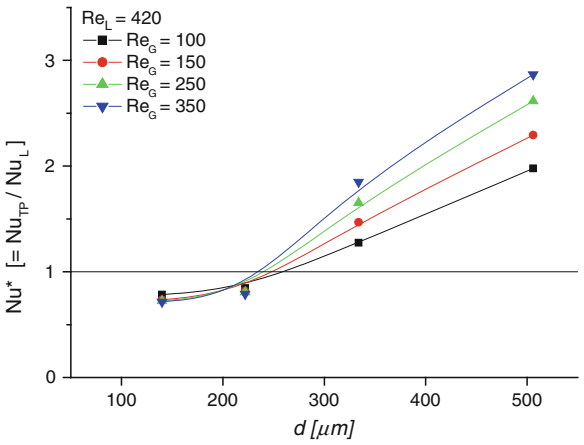

Fig. 1.26 Variation in Nusselt number with channel diameter, showing the transition diameter (Choo and Kim 2011)

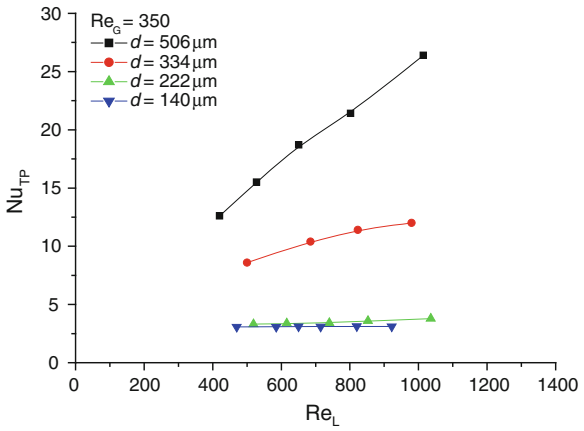

Fig. 1.27 Variation in Nusselt number with liquid flow rate at a fixed gas flow rate

The dimensionless channel diameter is defined by $d^* = d/(\sqrt{\sigma/pg})$. It is worth noting that the functional form of Eq. (1.48) was chosen to match the form of Eq. (1.47). As shown in Eq. (1.50a), the exponent m of Eq. (1.48) goes to 0 as the dimensionless channel diameter decreases. As shown in Fig. 1.27, this means that the effect of liquid flow rate (Re_L) is diminished as the dimensionless channel diameter decreases. However, the exponent m of Eq. (1.48) goes to 0.8 as the dimensionless channel diameter increases. As shown in Eq. (1.49), the factor F has a form similar to the previous correlation, Eq. (1.47). As shown in Eq. (1.50c), the exponent on the Martinelli parameter n in Eq. (1.49) becomes negative as the dimensionless channel diameter decreases. As shown in Fig. 1.21, at smaller channel diameters this means that the Nusselt number decreases with increasing gas flow rate (Re_G). However, the exponent n of Eq. (1.50c) goes to 0.7 as the dimensionless channel diameter increases. Therefore, the present correlation,

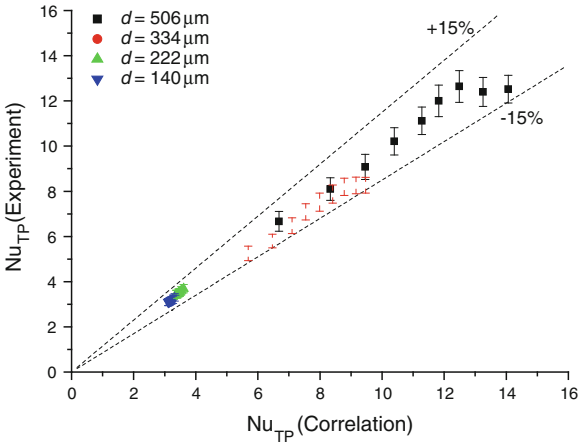

Fig. 1.28 Comparison between the Nusselt number obtained from the correlation of Eq. (1.43) and that from experimental results

Eq. (1.48), becomes identical to the previous correlation, Eq. (1.47), as the diameter becomes larger than 0.506 mm, as shown in Fig. 1.21. As shown in Fig. 1.28, the correlation of Eq. (1.48) for microchannels of diameter greater than 140 μm is well matched with the experimental results within ±15 %.